Journal of the Mechanics and Physics of Solids 142 (2020) 104012

Contents lists available at ScienceDirect

Journal of the Mechanics and Physics of Solids

journal homepage: www.elsevier.com/locate/jmps

Necking and drawing of rubber–plastic laminate composites: Finite element simulations and analytical model

Rahul G. Ramachandran[a], Spandan Maiti[a,b], Sachin S. Velankar[a,c,*]

[a] Department of Mechanical Engineering and Materials Science, University of Pittsburgh, Pittsburgh, PA, United States
[b] Department of Bioengineering, University of Pittsburgh, Pittsburgh, PA, United States
[c] Department of Chemical Engineering, University of Pittsburgh, Pittsburgh, PA, United States

ARTICLE INFO

Article history:
Received 27 November 2019
Revised 25 March 2020
Accepted 26 April 2020
Available online 25 May 2020

Keywords:
Necking
Drawing
Strain hardening
Layered composites
Toughening

ABSTRACT

Many plastics show necking and drawing behavior in tension, sometimes called "cold drawing". In contrast, elastomers stretch homogeneously in tension. We examine the tensile behavior of rubber–plastic laminate composites using 3D finite element simulations and an analytical model. A rate-independent constitutive behavior was adopted in which the modulus at small-strain, strain hardening at large strain, and yield stress (only for the plastic) can all be varied independently. For sufficiently small rubber/plastic thickness ratio, layered composites show necking and drawing wherein a tensile bar coexists in two strain states, one with a large stretch (necked region) and the other with a modest stretch (unnecked region). With increasing rubber/plastic thickness ratio, the two strain states approach each other in a manner resembling a second order phase transition culminating in a critical point. Above this critical rubber/plastic thickness ratio, the layered composites stretch homogeneously. An analytical model based on adding the First Piola–Kirchoff stresses of the rubber and plastic layers, along with a modification for inelastic deformation, is shown to capture most of the results of 3D simulations accurately. We comment on the practical relevance of these results to toughening relatively brittle plastics, and more specifically, the critical importance of strain hardening of the rubber.

Contents

* Corresponding author at: Department of Chemical Engineering, University of Pittsburgh, Pittsburgh, PA, United States.
E-mail address: velankar@pitt.edu (S.S. Velankar).

https://doi.org/10.1016/j.jmps.2020.104012
0022-5096/

1. Introduction

Many polymers show yielding behavior during deformation wherein the slope of the true stress–strain relationship decreases sharply at some stress, generally called the yield stress (Argon, 2013b). However, when deformed to higher strain, some yielding polymers show strong strain hardening wherein the slope of the true stress–strain relationship increases again (Argon, 2013a). A macroscopic consequence of yielding followed by strain hardening is an inhomogeneous deformation behavior called "cold drawing": under tension, a bar of the polymer first develops a neck (Hutchinson and Miles, 1974), however, the deformation in the neck stagnates and then the neck propagates steadily along the length of the bar (Andrews and Ward, 1970; Barenblatt, 1974; Carothers and Hills, 1932; Vincent, 1960). In contrast, elastomers do not show yielding behavior and deform without necking, as may be verified readily by stretching a rubber band.

This article is about the behavior of layered composites of a cold drawing polymer and an elastomer. Composites comprising layers with distinct material properties have been found to exhibit exceptional properties. For instance, the tear strength of a brittle material can be improved by layering it with a compliant layer (Hutchinson, 2014). Bonding a layer of elastomer to a ductile metal can allow the layered composite to stretch a larger extent without necking, whereas the metal alone would neck to failure at only a small applied strain (Li et al., 2004; Lu et al., 2007). For example, a gold film deposited on elastomer was found to stretch 100% more without losing conductivity (Lambricht et al., 2013).

This paper is motivated by our recent experimental research (Ramachandran et al., 2018) on the large-deformation tensile behavior of bilayer composites comprising a cold drawing plastic layer (linear low-density polyethylene, LLDPE) bonded to an elastomer (styrene-ethylene/propylene-styrene, SEPS). Fig. 1A shows a snapshot of the tensile deformation of a dog bone shaped specimen of LLDPE undergoing cold drawing. The gauge section of the sample shows two distinct zones: a highly stretched necked region with a stretch of almost 6, and an unnecked region with a stretch of less than 1.2. In contrast, SEPS rubber (Fig. 1B) stretched without necking to a few hundred percent strain, as typical for elastomers. Fig. 1C is a bilayer laminate composite of SEPS and LLDPE whose behavior is intermediate between the plastic and the rubber: while it showed necking and drawing, the degree of non-homogeneity of deformation reduced as compared to the pure LLDPE. For such composites, deformation became increasingly homogeneous as the rubber/plastic thickness ratio increased, and the transition region between the necked and unnecked regions became much wider.

During drawing, the material in the necked region is subjected to a large true stress due to a significant reduction in cross-section area. Strain hardening in the plastic controls the cold drawing phenomenon (Bigg, 1976; Coates and Ward, 1978, 1980; Erickson, 1975; Gsell and Jonas, 1979; Hutchinson and Miles, 1974; Hutchinson and Neale, 1977; Vincent, 1960). This article focuses on the modifications to the large deformation of thin layers of cold drawing polymers due to the addition of a rubber layer. The goals of this study are as follows. First, we seek a clear understanding of the effects of the rubber modulus and the rubber strain hardening on the deformation. Specifically, the rubber modulus is expected to affect small deformation processes (e.g. neck initiation) whereas the rubber strain hardening behavior is expected to affect large deformation processes (e.g. neck propagation). To isolate these effects clearly, we adopt constitutive equations in which the low strain modulus, yielding behavior, and strain hardening can all be varied independently. Such independent control of various material properties is not possible experimentally. Second, we seek to test whether the predictions of an analytical model developed in our previous paper are valid, even approximately. Even though the model cannot give all details of the deformation during neck propagation, it readily predicts practically useful quantities such as the engineering stress needed for stable neck propagation, or the stretch within the necked region (sometimes called draw ratio). If these model predictions can be shown to agree with 3D simulations, the analytical model can be practically useful for design purposes, e.g. rapidly estimating the rubber/plastic ratio needed to eliminate necking, or estimating the maximum stress experienced in each layer.

This paper is organized as follows. Section 2 describes the constitutive equations used and the simulation methods. Section 3 discusses the simulation results of how rubber thickness affects the stress–strain behavior for one specific case of material properties. Section 4 discusses the analytical model to show that many of the important quantities obtained from

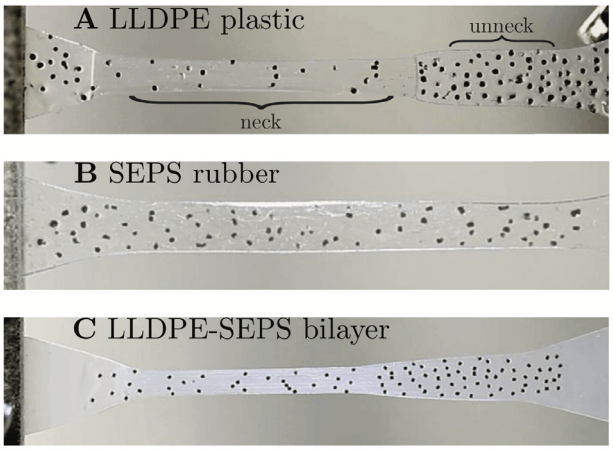

Fig. 1. Deformed shapes during tensile tests of dogbone-shaped samples of (A) Cold drawing LLDPE plastic (B) SEPS rubber which deforms uniformly throughout the gauge section. (C) SEPS - LLDPE bilayer of rubber/LLDPE thickness ratio of 1.2 (Ramachandran et al., 2018). Note the strongly non-homogeneous deformation in Fig. 1A where the necked region has a stretch of ~6, whereas the unnecked region has a stretch of less than 1.2. In contrast, the stretch in the necked region of the composite in Fig. 1C is lower, roughly 4.5. Increasing rubber thickness further reduced the stretch in the necked region(Ramachandran et al., 2018). The black dots are markers used for quantitative image analysis conducted previously(Ramachandran et al., 2018).

simulations can be predicted accurately and discusses the effect of inelastic deformation on the model predictions. Further, we conduct a parametric study to test how the material parameters of the rubber affect the initiation of necking and stable neck propagation. Finally, the practical relevance of these results to rubber-plastic laminates are discussed.

2. Methods

2.1. Constitutive modeling of rubber and cold drawing plastic

The rubber (denoted with the subscript r) was modeled as a rate-independent, isotropic, incompressible hyperelastic material. For our constitutive model, the behavior in uniaxial tension is:

$$\sigma_{\mathrm{r}}(\lambda) = \left[2\left(C_{1\mathrm{r}} + C_{2\mathrm{r}}\lambda^{-1}\right) + 4C_{3\mathrm{r}}\left(\lambda^2 - 2\lambda^{-1} - 3\right)\right]\left(\lambda^2 - \lambda^{-1}\right) \tag{1}$$

where σ_{r} is the *xx* component of the Cauchy stress of the rubber (true stress), λ (true stretch) is the uniaxial stretch along the *x* direction, and $C_{1\mathrm{r}}$, $C_{2\mathrm{r}}$, and $C_{3\mathrm{r}}$ are fitting parameters. The constitutive behavior for rubber in terms of the First Piola-Kirchoff (PK1) stress is given as:

$$P_{\mathrm{r}}(\lambda) = \frac{\sigma_{\mathrm{r}}}{\lambda} \tag{2}$$

The cold drawing plastic (denoted with the subscript p) was modeled as a rate-independent, isotropic, incompressible elasto-plastic material. For our constitutive model, the behavior in uniaxial tension is:

$$\sigma_{\mathrm{p}}(\lambda) = \begin{cases} 2C_{1\mathrm{p}}\left(\lambda^2 - \lambda^{-1}\right), & if\ \sigma_{\mathrm{p}} < \sigma_y \\ \sigma_y + H\bar{\epsilon}_p + 4C_{2\mathrm{p}}\left(\lambda^2 - 2\lambda^{-1} - 3\right)\left(\lambda^2 - \lambda^{-1}\right), & if\ \sigma_{\mathrm{p}} \geq \sigma_y \end{cases} \tag{3}$$

where σ_{p} is the *xx* component of the Cauchy stress of the plastic (true stress), σ_y is the yield stress, H is the coefficient of linear strain hardening and $C_{2\mathrm{p}}$ is the non-linear strain hardening coefficient. The plastic strain $\bar{\epsilon}_p$ is given as

$$\bar{\epsilon}_p(\lambda) = \ln\left(\frac{\lambda}{\lambda_y}\right) \ \forall\ \lambda > \lambda_y \tag{4}$$

where λ_y is the yield stretch obtained from setting $\sigma_{\mathrm{p}} = \sigma_y$ in Eq. (3). Once again, constitutive behavior of plastic in terms of PK1 stress can be obtained as:

$$P_{\mathrm{p}}(\lambda) = \frac{\sigma_{\mathrm{p}}}{\lambda} \tag{5}$$

3D form of the constitutive relations Eq. (1) and Eq. (3) for rubber and plastic were implemented in finite element simulations. Further details of the simulation procedure were published previously (Yang et al., 2017).

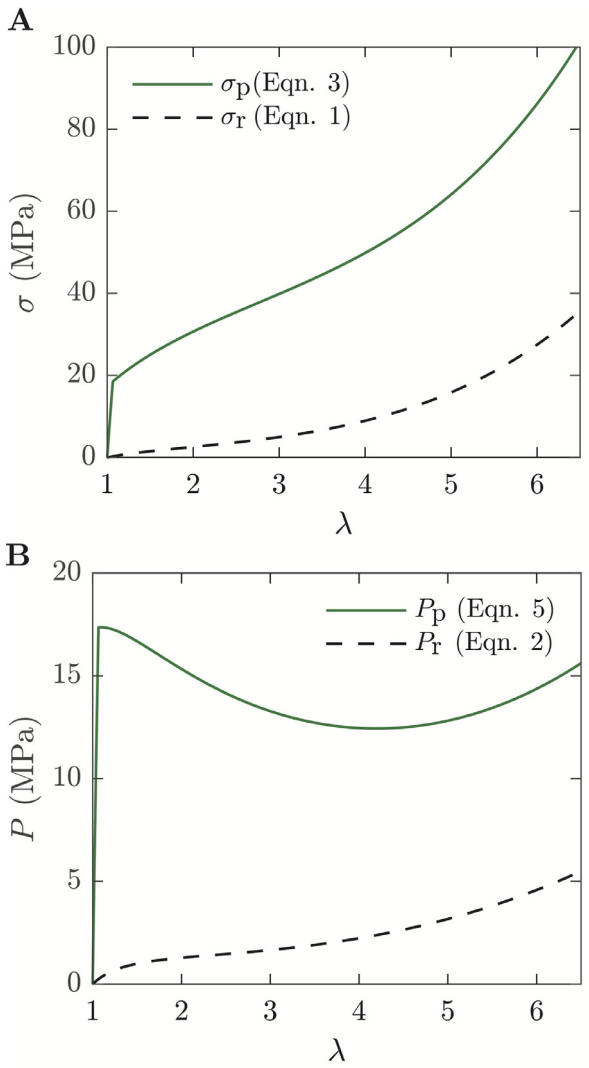

Fig. 2. Uniaxial constitutive behavior for the cold drawing plastic and the rubber (A) true stress ($\sigma - \lambda$ curve) (B) PK1 stress ($P - \lambda$ curve). PK1 stress in the plastic does not increase monotonically in contrast to rubber which increases monotonically.

2.2. Material parameters for the rubber and plastic

The material parameters of cold drawing polymer and hyperelastic rubber were calibrated by regressing simulated engineering stress-applied stretch curves against uniaxial experimental curves for LLDPE and SEPS rubber respectively. For the rubber, the simulated engineering stress with material parameter values $C_{1r} = 0$ MPa, C_{2r}= 0.7 MPa, and $C_{3r} = 0.004$ MPa yielded a good fit with experimental engineering stress-applied stretch behavior of SEPS (Appendix Fig. A2A). These values are used for most of the research in this paper. For the parametric analysis (Section 4.3), C_{1r} was kept unchanged, whereas C_{2r} was varied from 0.7 to 14.7 MPa, and C_{3r} was varied from 0 to 0.14 MPa.

For the cold drawing plastic, the engineering stress response from finite element simulation was calibrated against the experimentally obtained engineering stress response, as well as the experimentally measured draw ratio (i.e. the stretch in the neck during stable drawing), of LLDPE. The simulated engineering response with shear modulus, $2C_{1p} = 100$ MPa, the yield stress and the strain hardening parameters $\sigma_y = 18.4$ MPa, $H = 19$ MPa, and $C_{2p} = 0.0073$ MPa captured the experimental engineering stress-applied stretch response reasonably well as shown in the Electronic Supplementary Information (Appendix Fig. A2B). These values are used throughout this paper.

The constitutive behavior in terms of true stress ($\sigma - \lambda$ curve) and PK1 stress ($P - \lambda$ curve) for rubber and plastic with material parameter values given above are shown in Fig. 2. The key point to note is that the $P - \lambda$ curve increases monotonically for the rubber layer, but shows a maximum followed by a minimum for the plastic layer. This non-monotonic behavior is the crucial feature that induces necking and drawing as discussed later.

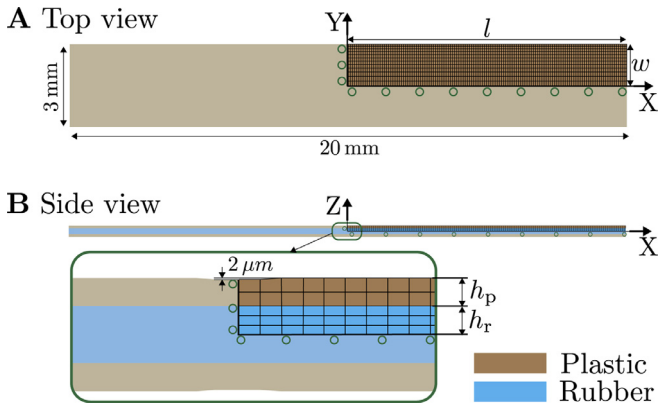

Fig. 3. The rectangular specimen geometry 20 × 3 mm. One-eighth of geometry is modeled with rollers (green open circles) applied along the $X = 0$, $Y = 0$, and $Z = 0$ planes. The thickness of the element along the center (in the X direction) is decreased by 2 μm to induce consistent neck initiation at the center.

2.3. Finite element model

Simulations were conducted using a custom nonlinear finite element program. One-eighth of the plastic/rubber/plastic trilayer specimen of rectangular cross-section was modeled to exploit the symmetry of the specimen. The computational model consisted of a single layer of plastic and rubber each, with length l =10 mm along the stretching direction, and width w = 1.5 mm along the transverse direction. This geometry mimics the gauge section of the tensile experiments of Fig. 1, although the experiments used bilayers rather than trilayers. The thickness of the plastic layer was kept at, $h_p = 100$ micron and the rubber thickness were varied from h_r= 100 to 800 μm. This corresponds to rubber/plastic thickness ratio (ω) defined as $\omega = h_r/h_p$, in the range from 1 to 8.0. The thickness of the array of elements (75 μm long in the stretching direction) on the top surface along the centerline in the plastic layer was reduced by 2 μm (see inset of Fig. 3) to consistently introduce necking at the midplane. Roller boundary conditions were enforced on adjoining faces in all three rectangular directions ($X = 0$, $Y = 0$, and $Z = 0$ planes), as marked by green circles in the top and side view (Fig. 3A and B). The rubber and the plastic faces with $X = l$ (rightmost edge in Fig. 3B) were displaced stepwise along x-direction to stretch the sample, whereas the surfaces $Y = w$ and $Z = h_p + h_r$ were specified as stress-free.

The representative computational model of the trilayer was meshed using 8-noded brick elements. Each material layer contained at least 2 elements in the thickness direction with 1330 elements in each layer (mesh shown in Fig. 3). The ratio of the deformed length ($\delta + l$) to the original length l is defined as the applied stretch, $\lambda_{app} = 1 + \frac{\delta}{l}$ where δ is the applied displacement. A stretch of 6.5 was applied at the right end in 7000 steps. Stretch, plastic strain and effective stress contours were enumerated at an interval of 20 steps over the specimen volume. The stretch and stress distribution monitored on the top free surface ($Z = h_r + h_p$) are shown in Section 3. Reaction forces were measured at all the nodes on the midplane along the length of the specimen ($X = 0$ plane), which is the symmetry plane that acts as a boundary of the simulation domain. The engineering stress (N) over the composite is calculated by: $N = \frac{F}{A_0} = \frac{F}{w(h_r+h_p)}$. where F is the sum of current reaction forces in all the nodes along the midplane ($X = 0$ plane) and $A_0 = w(h_r + h_p)$ is the cross-section area in the undeformed state.

3. Results

Section 3.1 discusses the deformation of free-standing rubber and cold drawing plastic from finite element simulations. Section 3.2 discusses rubber-plastic trilayer composites for different ω values.

3.1. Deformation of free-standing plastic and rubber

The engineering stress in uniaxial tension from finite element simulations for the rubber and the cold drawing plastic is shown in Fig. 4A. The corresponding deformed configurations at λ_{app} values of 1, 1.5, 3 and 6 are shown in Fig. 4B and C respectively. The color map shows the stretch distribution in the longitudinal direction. The Von Mises stress (σ_e) distribution at λ_{app}=3 for the rubber and cold drawing plastic are shown in Fig. 4D and E, respectively.

For the rubber, the engineering stress vs applied stretch ($N - \lambda_{app}$ curve) increases monotonically (Fig. 4A), and Fig. 4B shows that the deformation remains homogeneous, i.e. at all locations within the sample, the stretch value in the longitudinal direction is equal to the applied stretch. Due to chosen boundary conditions, the stress field is uniform under uniaxial loading, as indicated in Fig. 4D. Furthermore, although not shown in Fig. 4A, the engineering stress agrees almost exactly with the PK1 stress, $P_r(\lambda)$ (Eqn. (2)), which was already shown in Fig. 2B.

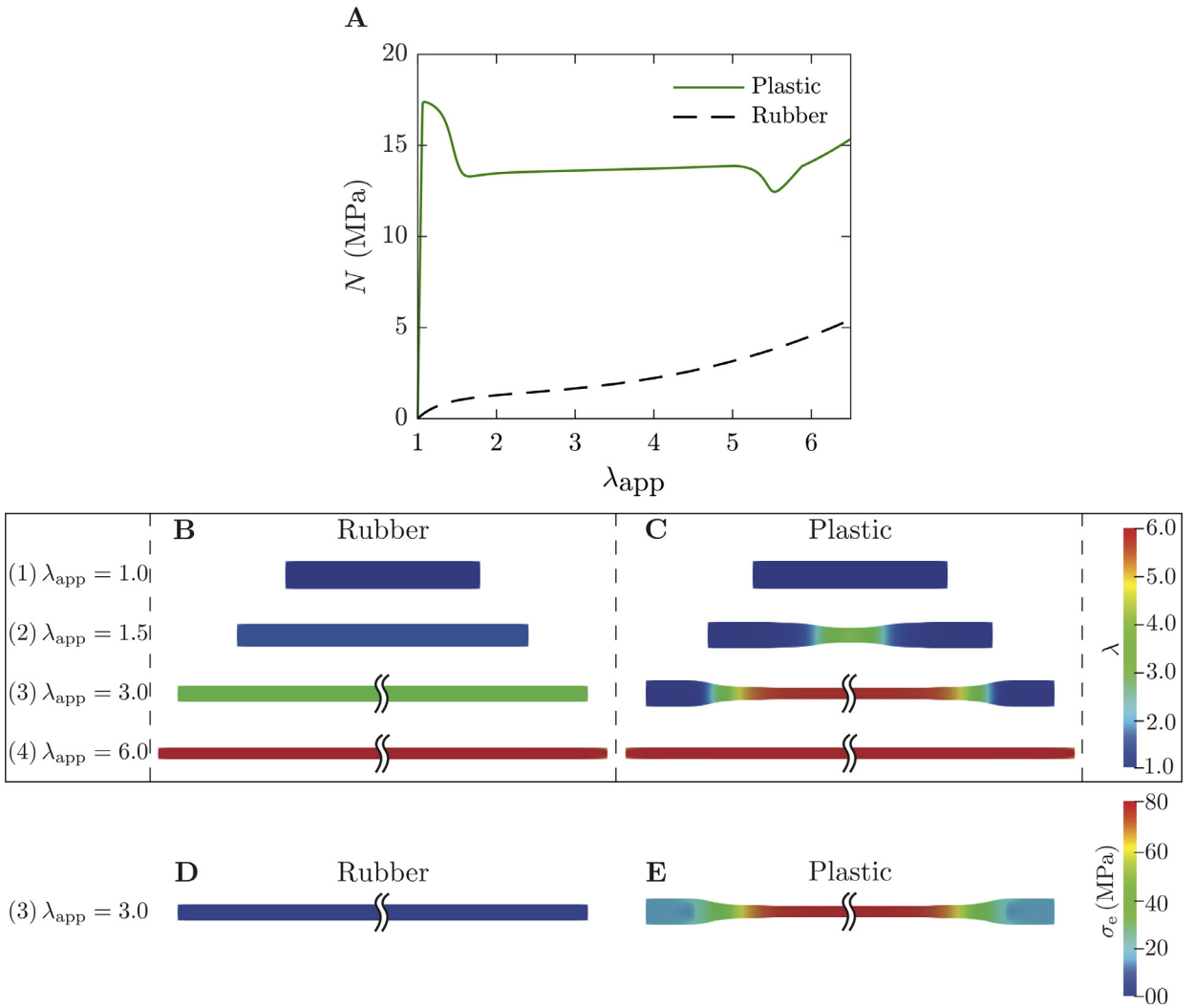

Fig. 4. (A). Engineering stress vs applied stretch ($N - \lambda_{app}$ curve) from simulations of rubber and cold drawing plastic. Initial configuration and deformed configurations for (B) the rubber and (C) the cold drawing plastic. Numbers far left indicate applied stretch (λ_{app}) values for each configuration, and contours indicate the distribution of stretch in the tensile direction. Deformed configuration with color map of Von Mises stress, σ_e at an applied stretch (λ_{app}) of 3 for the rubber (D) and the cold drawing plastic (E).

In contrast, for the free-standing plastic, the $N - \lambda_{app}$ curve does not increase monotonically (Fig. 4A). The deformation of the plastic, as shown in Fig. 4C is non-homogeneous. The specimen stretches uniformly up to a stretch of 1.12, upon which a neck initiates at the center, and the engineering stress reduces sharply. The neck then stretches locally, whereas the material outside the neck stays at a lower stretch. This state is illustrated at $\lambda_{app} = 1.5$ in Fig. 4C. In concert, the engineering stress reduces towards a plateau at draw stress of $N_{draw} \approx 13$ MPa. The configuration at $\lambda_{app} = 3$ in Fig. 4C shows the deformed shape typical of a specimen within the engineering stress plateau where three distinct regions can be identified. The first is the necked region near the center which has a large stretch ($\lambda_{neck} \approx 5.9$) compared to the rest of the geometry. The second is the unnecked region where the material remains in nearly the same state prior to necking, with a local stretch of $\lambda_{unneck} \approx 1.1$. The third is the transition region between the aforementioned regions, where the value of the stretch smoothly transitions from the value in necked region to the value in the unnecked region. Similar to the stretch distribution, the stress within this sample is also non-homogeneous as indicated in Fig. 4E. The stress is maximum in the neck with a value of 80 MPa.

These three regions do not change significantly with λ_{app} throughout the engineering stress plateau; the sole change is the increase in the length of the necked region at the expense of the unnecked region. Thus, this regime of stretching corresponds to stable drawing or stable neck propagation. Finally, at $\lambda_{app} = 5.9$ the necked state spans the entire specimen, beyond which the sample stretches homogeneously.

Incidentally, the dip in stress seen at $\lambda_{app} \approx 5.5$ is due to the geometric softening when the neck reaches the edge of the specimen. The reduction in cross-section of the transition zone reduces the force required to sustain tensile deformation.

Such a dip is an artifact of the rectangular simulation geometry and would not be seen experimentally when dog-bone shaped specimens are used.

Unlike the rubber which deforms homogeneously, for the cold drawing plastic, the $N - \lambda_{app}$ curve distinctly deviates from the $P - \lambda$ relation. Analytical prediction of some of the features of $N - \lambda_{app}$ curve from the $P - \lambda$ relation is discussed in Section 4.

3.2. Deformation of rubber/plastic laminates

The engineering stress response ($N - \lambda_{app}$ curve) of laminate composites with ω =1, 3 and 7 are shown in Fig. 5A. The curves for the free-standing plastic layer ($\omega = 0$) and the free-standing rubber, which were shown in Fig. 4A, are also shown for reference. The deformed shapes at a λ_{app} =3 for the specimens are shown in Fig. 5B. The color maps indicate the local stretch in the x-direction. For $\omega = 1$ and 3, the engineering stress exhibits a peak, followed by a plateau, both typical of necking and stable drawing behavior. The corresponding deformed shapes clearly show non-homogeneous deformation. The stretch maps indicate that with increasing ω, the stretch in the neck λ_{neck} decreases and the stretch in the unnecked region λ_{unneck} increases. For a fixed ω value the λ_{neck} and λ_{unneck} remain constant throughout the neck propagation, similar to the free-standing plastic in Fig. 4B. All these trends agree with our previous experimental observations (Ramachandran et al., 2018). For $\omega = 7$, necking is eliminated completely as judged by both, the monotonic rise on N with $\lambda_{app,}$ as well as by the uniform stretch distribution.

It is interesting to compare the simulated behavior of the composite against a thickness-weighted sum of the force in each free-standing layer. However, such force additivity of the free-standing rubber and plastic does not capture the entire stress-stretch behavior of the laminate composite accurately. This issue is discussed further in the Supplementary Information along with Fig. A1.

To further emphasize this issue of different strain states, Fig. 5C plots the Cauchy stress and the stretch of the individual layers within the composites in the necked and unnecked region. The solid and dashed curves represent the constitutive behavior of the plastic and the rubber in uniaxial tension respectively (Eqs. (3) and (1)). The circles on the solid curve mark the true stress in the necked and unnecked region for free-standing plastic, with the larger value of stress corresponding to the necked region. With increase in ω, the true stress in the necked region decreases. This plot shows that the plastic layers in the composites experience lower stress and therefore experience deformation states that are inaccessible to the free-standing plastic during drawing.

Another significant effect is that the increase in ω delays the peak in engineering stress-stretch response (λ_{peak}) to a larger applied stretch. Yet the yield strain in the plastic layer of the composite remains a constant since it is a material property. Therefore increasing ω increases the inelastic deformation in the plastic material at the onset of necking. This is illustrated more clearly in Fig. 6, which plots the plastic strain at the onset of necking; it is clear that when bonded to rubber, the plastic layer can undergo large plastic deformation before necking. This same point was made previously by Li et al. (2005), albeit with a plastic that was not capable of cold drawing. The central point, therefore, is that bonding together the rubber and the plastic forces the individual materials to stretch in a fashion that is different from the same materials when stretched alone.

Four key quantities of practical interest, λ_{peak}, N_{draw}, λ_{neck}, and λ_{unneck} can be extracted readily from the simulations. The first two can be extracted directly from the engineering stress data: the stretch corresponding to the peak in engineering stress, λ_{peak}, which marks the onset of necking, and the engineering stress, N_{draw} for stable drawing, corresponding to the stress plateau. The increase in λ_{peak} with ω is shown in Fig. 7A, whereas the decrease in N_{draw} with ω is shown in Fig. 7B. λ_{neck} and λ_{unneck} can be obtained from the deformed configurations. To do this in a consistent fashion for all samples, we plot the highest and the lowest stretch within each specimen during stretching (see Appendix Fig. A3) and extract the two plateau values which correspond to stable drawing. The two quantities are plotted vs the rubber/plastic ratio ω in Fig. 7C. Such plots depend on the material properties, and Section 4.2 will show similar plots for laminate composites with different parameter values in the material constitutive equations. The solid curves in Fig. 7 will be discussed later.

4. Analytical model

The central phenomenon of interest in this paper is the coexistence of two strain states during stable drawing and the changes in these states as rubber thickness changes. We extend the Maxwell analysis, which identifies the two coexisting states(Coleman, 1983; Erickson, 1975; Fager and Bassani, 1986; Hutchinson and Neale, 1983; Neale and Tugcu, 1985), to the tensile deformation of the composites. Unlike our previous paper(Ramachandran et al., 2018), we will focus on the energy of the system to make more explicit the analog to phase transition phenomenon familiar from thermodynamics and to make more transparent the issue of inelastic deformation that was ignored previously.

4.1. Comparison against energy-based 1D model

It is well-recognized that in uniaxial elongation of a bar, if the $P - \lambda$ curve shows a maximum, a neck initiates at the stretch corresponding to the maximum (Considère, 1885; Courtney, 1990). Stable neck propagation further requires that the $P - \lambda$ curve also has a minimum (Coleman, 1983; Erickson, 1975; Neale and Tugcu, 1985). Fig. 8A therefore illustrates a $P - \lambda$

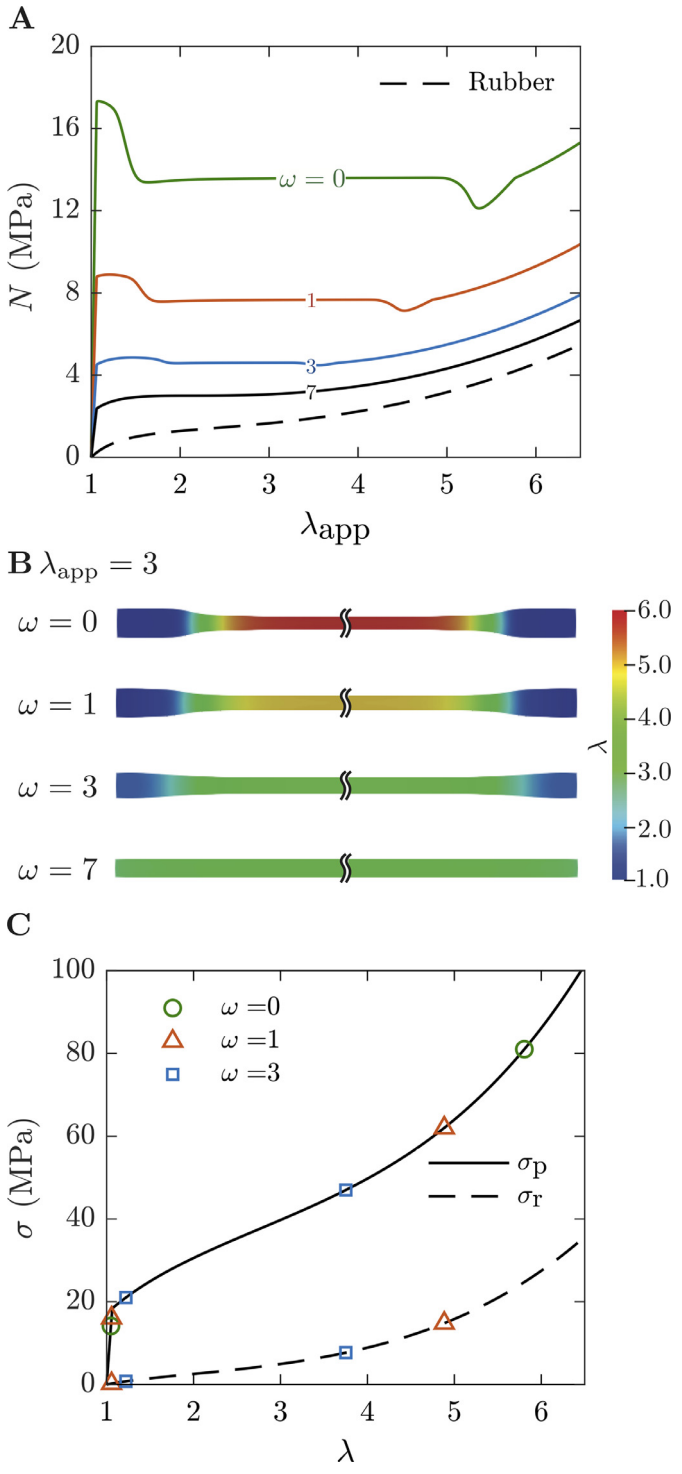

Fig. 5. (A) Engineering stress vs applied stretch ($N - \lambda_{app}$) response of layered composites with rubber/plastic ratios (ω) listed alongside each curve. (B) The deformed configurations at $\lambda_{app} = 3$ for free-standing plastic ($\omega = 0$) and composites of ω values listed on the left of each image. Laminates with $\omega = 1$ and 3 show drawing behavior, but the stretch in the neck (λ_{neck}) decreases with increasing ω. (C) The true stress in the necked and unnecked regions of individual layers of composites are marked on the respective true stress vs true stretch ($\sigma - \lambda$) curve. Solid and dashed lines are the $\sigma - \lambda$ for the rubber and plastic, Eqs. (1) and (3), respectively. The green circles mark the true stress in the necked and unnecked region in free-standing plastic during neck propagation, whereas the red triangles and blue squares mark the true stress in the necked and unnecked region in the rubber and plastic layer in laminate composites of ω values of 1 and 3 respectively.

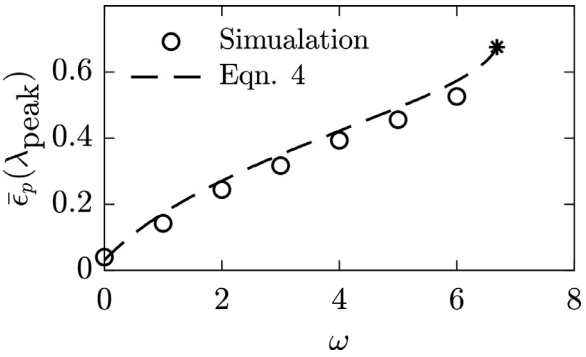

Fig. 6. Effective plastic strain from the 3D simulations at the onset of necking is shown as open circles. The dashed line corresponds to substituting the prediction for $\lambda = \lambda_{peak}$ from Eqn. (7) into Eqn. (4).

curve showing such a maximum followed by a minimum. In previous analyses of stable neck propagation (Coleman, 1983; Erickson, 1975; Hutchinson and Neale, 1983), the cold drawing material was assumed to have a fictitious non-linear elastic sigmoidal stress-stretch response, and a Maxwell equal area construction was then developed to identify the two coexisting strain states that correspond to stable drawing. This construction is illustrated as a dashed green line in Fig. 8A, where points *b* and *c* correspond to the unnecked and necked states respectively, and the shaded areas are equal. Prediction from Maxwell analysis has been compared against experiments previously and found to be in reasonable agreement (Crist and Metaxas, 2004).

The total area under the $P-\lambda$ curve is proportional to the work done in deforming the sample to any desired applied stretch, λ_{app}. Within the energy-conservation framework, this corresponds to the strain energy density, W

$$W = \int_1^{\lambda_{app}} P\, d\lambda \tag{6}$$

It is illuminating to illustrate the deformation process on a W vs λ_{app} diagram (Fig. 8B), which closely resembles the energy vs order parameter diagrams commonly used in the study of phase transitions. Coexistence between the necked and unnecked states can now be identified by the familiar double-tangent construction for first-order phase transitions. This double-tangent makes it obvious that for λ_{app} values between those of points *b* and *c*, a specimen with two coexisting strain states can have lower energy than a specimen that stays homogeneous. The region between points *b* and *a* is metastable: while a specimen may remain in a homogeneous strain state, the separation between two coexisting strain states can reduce the energy to the value indicated by the double tangent. Such metastable states, e.g. supercooled liquids, are well-known amongst phase transitions. Thus, when stretching a bar of the material, necking initiates when the specimen is stretched to point *a*; once the neck is initiated, the stress must reduce to the level indicated by the Maxwell construction while the sample bifurcates into unnecked and necked regions in states *b* and *c* respectively. This decrease in stress is accompanied by a decrease in energy, indicated by a downward arrow in Fig. 8B.

The schematic of Fig. 8 applies for any specimen capable of stable drawing in tension. To apply it quantitatively to layered composites, an expression is needed for the $P-\lambda$ curve. We adopt a simple expression of thickness-weighted stress additivity:

$$P = P_p\left(\frac{1}{\omega+1}\right) + P_r\left(\frac{\omega}{\omega+1}\right) \tag{7}$$

It must be emphasized that Eq. (7) adds the nominal stresses under homogenous deformation. Eq. (A1) in the Appendix discusses a different version which adds forces from the free-standing layer.

Using the analytical expressions from Eqs. (2) and (5), the $P-\lambda$ curve for the laminate composite can be calculated from Eq. (7). Plots of Eq. (7) for various values of ω are shown in Fig. 9. For small values of ω, this equation is non-monotonic. The maximum then gives the stretch, λ_{peak}, at which a neck initiates. Further, the Maxwell construction identifies λ_{neck}, λ_{unneck}, (the red and blue squares respectively) and the draw stress, N_{draw} (PK1 stress corresponding to horizontal green dashed line). This Maxwell construction implemented using MATLAB®, is also illustrated in Fig. 9. For $\omega \geq 6.7$, *P* increases monotonically with λ, i.e. it is no longer possible to initiate necking. The corresponding predictions for stable neck propagation are shown as solid lines in Fig. 7: these correspond to the location of the maximum of Eq. (7) in Fig. 7A, and the results of the Maxwell construction in Fig. 7B and C.

There is an obvious resemblance of Fig. 7C to second-order phase transitions, e.g. gas-liquid coexistence near the critical point, liquid-liquid coexistence near the consolute point or the ferromagnetic transition near the Curie point. For the specific material parameters selected here, the critical value of rubber thickness, i.e. the value above which $P(\lambda)$ becomes monotonic, corresponds to $\omega_c = 6.7$. Indeed, Appendix Fig. A4 plots the results in the form suggested from the critical phenomena literature and shows that $(\lambda_{neck} - \lambda_{unneck}) \propto (\omega_c - \omega)^{\beta}$. The critical exponent β is found to be 0.54, a value close to 0.5, predicted from the mean-field theory of critical phenomena.

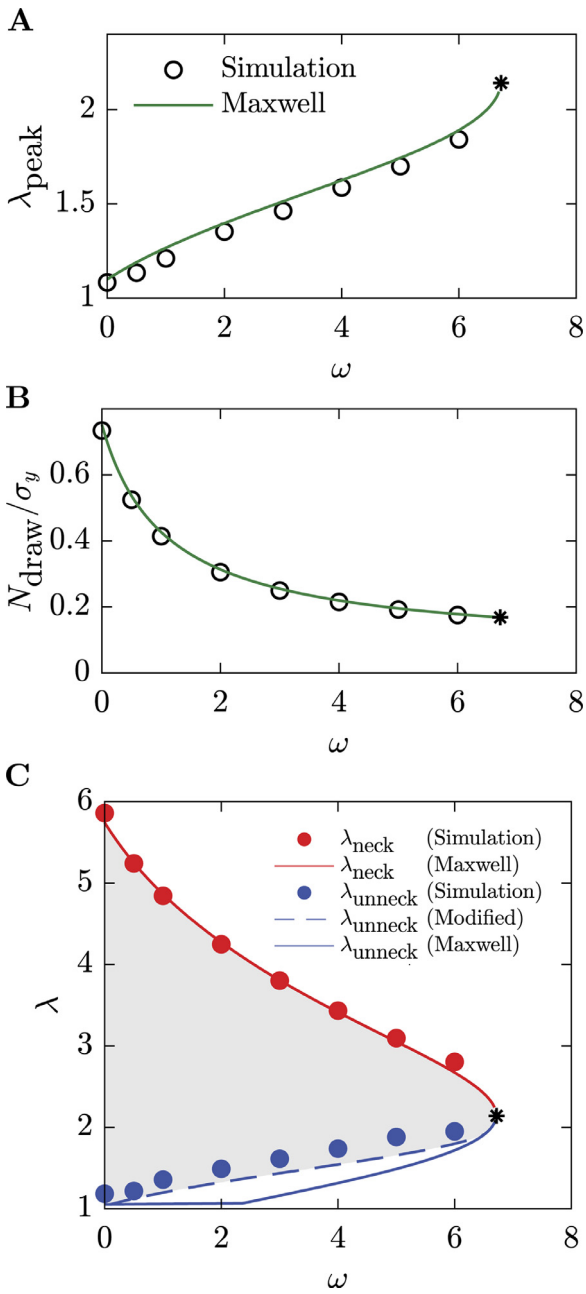

Fig. 7. (A) Open circles are stretch values at which simulations show a peak in engineering stress. (B) Open circles are engineering draw stress (normalized by the yield stress) from simulations. (C) Filled circles are simulation results for the stretch in the necked and unnecked regions (λ_{neck} and λ_{unneck}) during stable drawing. Solid lines are predictions: in (A) solid curve is the λ at which $P-\lambda$ curve of composites (Eq. (7)) shows a peak, at any value of ω. In (B) and (C) solid curves are the predictions of N_{draw} (normalized by σ_y), λ_{neck} and λ_{unneck} by applying Maxwell construction to Eq. (7) (see Fig. 9). The dashed line in (C) is the prediction for λ_{unneck} after correcting for inelastic deformation effects (see text and Fig. 10). In all graphs, the asterisk is the critical point, i.e. the lowest ω value (ω_c) needed for the $P(\lambda)$ from Eq. (7) to be monotonically increasing.

As mentioned in the Introduction, one key goal of this paper was to examine whether the analytical model of Eq. (7), combined with the Maxwell construction, can predict the key quantities obtained from the simulations. If so, the model can give rapid predictions for composite behavior based on pure component properties without needing detailed simulations. The solid curves in Fig. 7 suggest that the model can predict all quantities well, except λ_{unneck} which is significantly underpredicted. Section 4.3 will show that the degree of the underprediction of λ_{unneck} depends on the material properties. The following section examines the reasons for the underprediction.

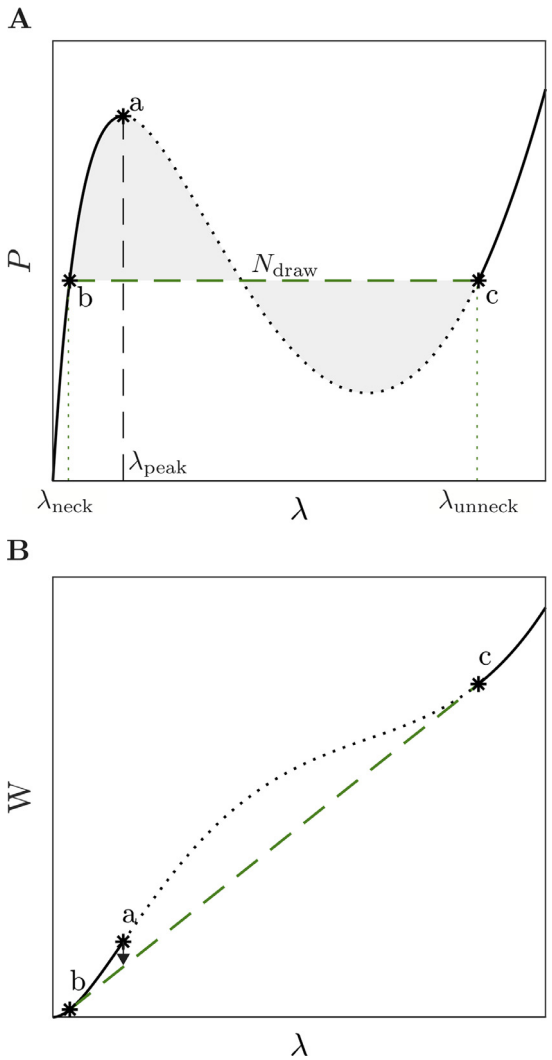

Fig. 8. (A) Schematic of a $P-\lambda$ curve with a maximum and minimum, which can show stable neck propagation. The neck initiates at the peak load (marker *a*). Constant PK1 stress dashed green line (N_{draw}) corresponds to the Maxwell construction where the two shaded areas are equal. Points *b* and *c* correspond to material states in the unnecked and necked region during stable neck propagation. (B) Strain energy per unit volume corresponding to constitutive behavior shown in Fig. 8A. The dashed green line is a double tangent to the W(λ) curve. The black dotted curves in both figures correspond to unstable regions where homogeneous deformation is not possible.

4.2. Irreversible deformation effects

The effect of irreversible deformation of the cold drawing plastic layer on the prediction of material configuration in the unneck region of the composite is discussed below. For illustrative purposes, most of the calculations in this section are done for a rubber-plastic composite of $\omega = 3.5$. The $P-\lambda$ curve calculated from Eq. (7), with $\omega = 3.5$, is shown in Fig. 10A. As explained along with the discussion of Fig. 8 above, during initial stretching, the neck initiates at the maximum in the $P-\lambda$ curve, marked *a* . As per the Maxwell construction, stable neck propagation requires lower engineering stress. This decrease in engineering stress after point *a* must be accompanied by a decrease in the stretch in the unnecked region. In a purely elastic system, the stretch of the unnecked region can recover from point *a* to point *b*, and in this final state, both layers would still remain under tension. However, with plasticity effects, i.e. irreversible deformation, the situation is different: if $\lambda_a - \lambda_b > \epsilon_y$, the plastic layer would lose tension altogether and experience compression. Further if $\lambda_a - \lambda_b > 2\epsilon_y$, the plastic would have to yield in compression. Here $\epsilon_y = \lambda_y - 1$ is the yield strain of the cold drawing material. The rubber in the unnecked region may not have sufficient elastic energy to accomplish the work necessary to force this compressive deformation. Therefore, the actual stretch of the unnecked region, λ_d would exceed λ_b. The goal of this section is to estimate λ_d through an energy analysis that accounts for irreversible work done.

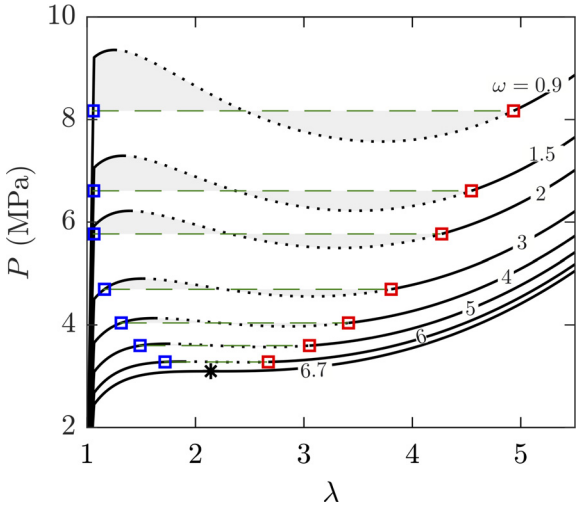

Fig. 9. $P-\lambda$ curves for composites (Eq. (7)) of various ω values indicated for each curve. Dotted regions of each curve correspond to regions where homogeneous stretching is not possible. Dashed green lines show Maxwell constructions where the shaded areas above and below each green line are equal. The material configurations in the necked and the unnecked regions are marked as the red and blue squares respectively on each $P-\lambda$ curve. The $P-\lambda$ curve is monotonic for laminate composites with $\omega >$ 6.7 (not shown here).

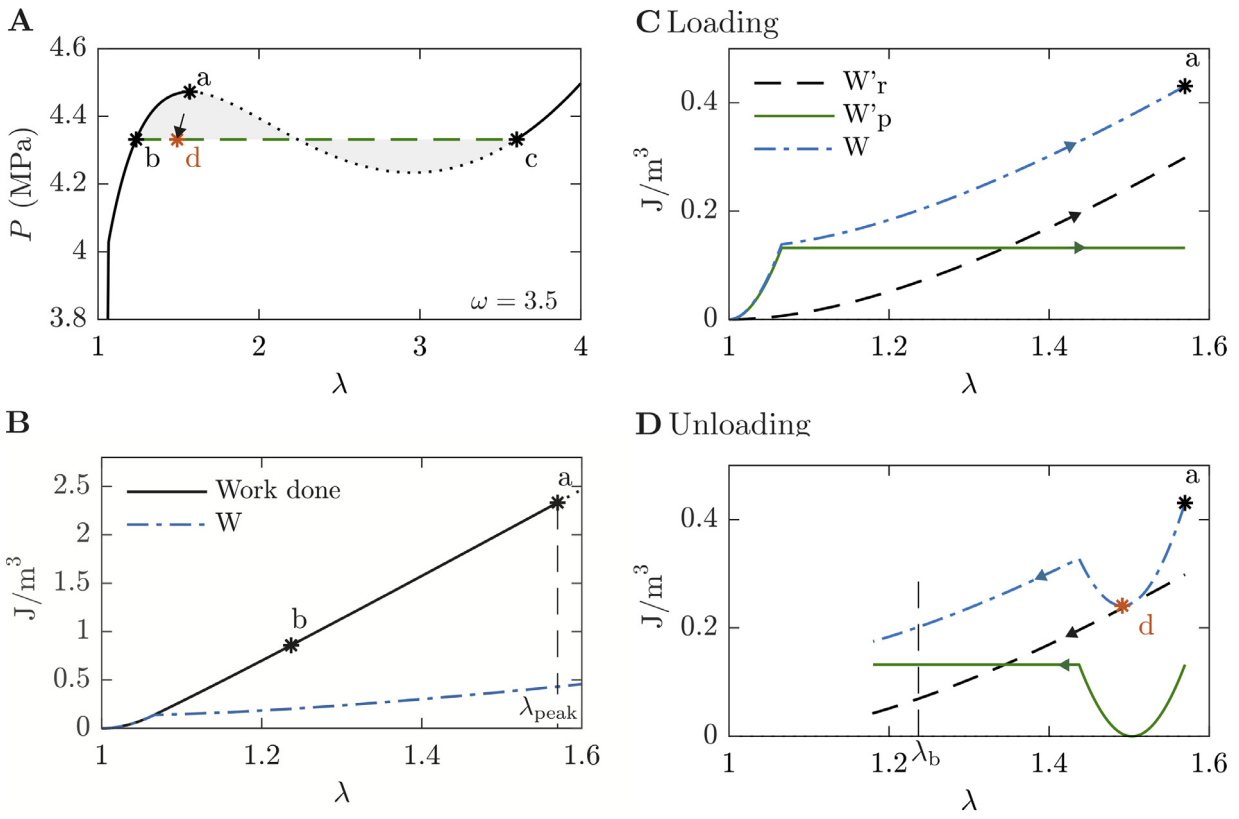

Fig. 10. (A) $P-\lambda$ curve for the rubber–plastic laminate of $\omega = 3.5$ (Eq. (7)). Maxwell construction is indicated by the green dashed, constant PK1 stress line. The points b and c where the Maxwell construction intersects the $P-\lambda$ curve are the predictions for material states in necked and unnecked regions. The material state in the unnecked region after considering the inelastic deformation of is marked as d. The dashed arrow linking a and d is indicative only. (B) Loading from $\lambda = 1$ to $\lambda = \lambda_a$. The black curve is the work done per unit volume of the composite, i.e. the area under the $P-\lambda$ curve in A. Blue dot-dashed line is the total strain energy density (Eqn. (8)). (C) Strain energy density when loading from $\lambda = 1$ to $\lambda = \lambda_a$. Plastic contribution (green) and rubber contribution (black dashed), their sum (blue dot-dashed, which is the same curve as in B). (D) Strain energy density when unloading from $\lambda = \lambda_a$.

For the following analysis, the composite is treated as a single material with uniform properties. The strain energy density of the composite is computed by the volume fraction-weighted sum of rubber and plastic strain energy density during loading and unloading. Loading and unloading are considered separately due to path dependence of the cold drawing material.

Therefore, we now write the total strain energy in the layered composite as a sum of contributions from the rubber and the plastic:

$$wl(h_r + h_p)W(\lambda) = wlh_r W_r(\lambda) + wlh_p W_p(\lambda)$$

$$\text{Hence } W(\lambda) = \frac{\omega}{\omega+1} W_r(\lambda) + \frac{1}{\omega+1} W_p(\lambda)$$

$$W(\lambda) = W_r'(\lambda) + W_p'(\lambda) \tag{8}$$

where w and l are the width and length of the specimen, respectively. $W_r'(\lambda) = \frac{\omega}{\omega+1} W_r(\lambda)$ is the rubber contribution to the strain energy density of the laminate composite, and similarly, $W_p'(\lambda) = \frac{1}{\omega+1} W_p(\lambda)$ is the plastic contribution to the strain energy density of the laminate composite.

During the loading process, for the rubber layer, all the work is presumed to be reversible, and hence is stored as elastic energy:

$$W_r(\lambda) = \int_1^{\lambda} P_r(\lambda) d\lambda \tag{9}$$

In contrast, for the plastic, only the work done prior to yielding is taken to be reversible. Thus, the plastic strain energy density is given as:

$$W_p(\lambda) = \begin{cases} \int_1^{\lambda} P_p(\lambda) d\lambda, & if\ \lambda < \lambda_y \\ \int_1^{\lambda_y} P_p(\lambda) d\lambda, & if\ \lambda \geq \lambda_y \end{cases} \tag{10}$$

From the above equations, W_r', W_p', and their sum $W(\lambda)$, during the loading process can be calculated readily and the values for $\omega = 3.5$ are shown in Fig. 10C. It is important to note that the latter integral in Eq. (10) is independent of λ, i.e. beyond the yield point, the plastic makes no further contribution to elastic energy. Therefore W_p' becomes horizontal for stretch larger than λ_y in Fig. 10C. The strain energy density of the composite, $W(\lambda)$ and the work done per unit volume up to the $P - \lambda$ curve peak (marker a) are shown in Fig. 10B. At the onset of necking, the work done per unit volume of the composite far exceeds the strain energy density.

We now turn to the unloading process in which the λ reduces starting from point a. To proceed, it is convenient to define $\Delta\epsilon = \lambda - \lambda_a$, i.e. the decrease in strain after the neck initiates, and $\epsilon_y = \lambda_y - 1$ as the yield strain. Since the rubber is elastic, its loading and unloading is not path dependent. Hence the rubber contribution to the strain energy density of the laminate during unloading is $W_r'(\lambda_a - \Delta\epsilon)$ from Eq. (9). The plastic contribution to the strain energy density of the laminate during unloading is path dependent and given as:

$$W_p(\lambda) = \begin{cases} W_p(\lambda_a) - \int_{1+\epsilon_y}^{1+\epsilon_y-\Delta\epsilon} P_p(\lambda) d\lambda, & if\ \Delta\epsilon < (\epsilon_y) \\ \int_1^{1+(\Delta\epsilon-\epsilon_y)} P_p(\lambda) d\lambda, & if\ (\epsilon_y) \leq \Delta\epsilon < 2(\epsilon_y) \\ \int_1^{1+\epsilon_y} P_p(\lambda) d\lambda, & if\ \Delta\epsilon \geq 2(\epsilon_y) \end{cases} \tag{11}$$

Eq. (11) can be understood as follows: As the stretch decreases below λ_a, the plastic layer first reduces its strain energy density while remaining under tension. At $\Delta\epsilon = \epsilon_y$, the plastic completely loses tension and its strain energy density is zero. Further increase in $\Delta\epsilon$ forces the plastic into compressive deformation, and the strain energy density increases. Once $\Delta\epsilon$ reaches $2\epsilon_y$, the plastic yields in compression, after which there is no further increase in strain energy density. This process is represented by the U-shaped green curve in Fig. 10D. The total strain energy in the composite during unloading can be found by adding the plastic and the rubber contributions (Eq. (8)), and is shown as the U-shaped blue dot-dashed curve. The minimum in this blue dot-dashed curve is now the predicted value of the stretch λ_d of the unnecked state. The point d is also marked in Fig. 10A. The dashed arrow linking a and d is only for illustration, and not quantitative.

The calculation illustrated in Fig. 10 was done for several ω values to obtain a prediction for λ_{unneck} which is shown as the dashed blue line in Fig. 7C. It is in reasonable agreement with the λ_{unneck} obtained from simulations suggesting that the above model can successfully capture the effects of inelastic deformation. We emphasize that this updated prediction still relies on Eq. (7), but it no longer uses the Maxwell construction.

4.3. Effect of rubber parameters

Simulations were conducted varying the two parameters C_{2r} and C_{3r} which define the constitutive behavior of the rubber (C_{1r} was still kept at zero). These simulations were done only at an equal thickness of the rubber and plastic layers, i.e. at $\omega = 1$. Fig. 11 shows the engineering stress curves and the corresponding deformed shapes as C_{2r} or C_{3r} are increased, holding all the other parameters constant. Qualitatively, the effect of changing these parameters is similar to that of changing

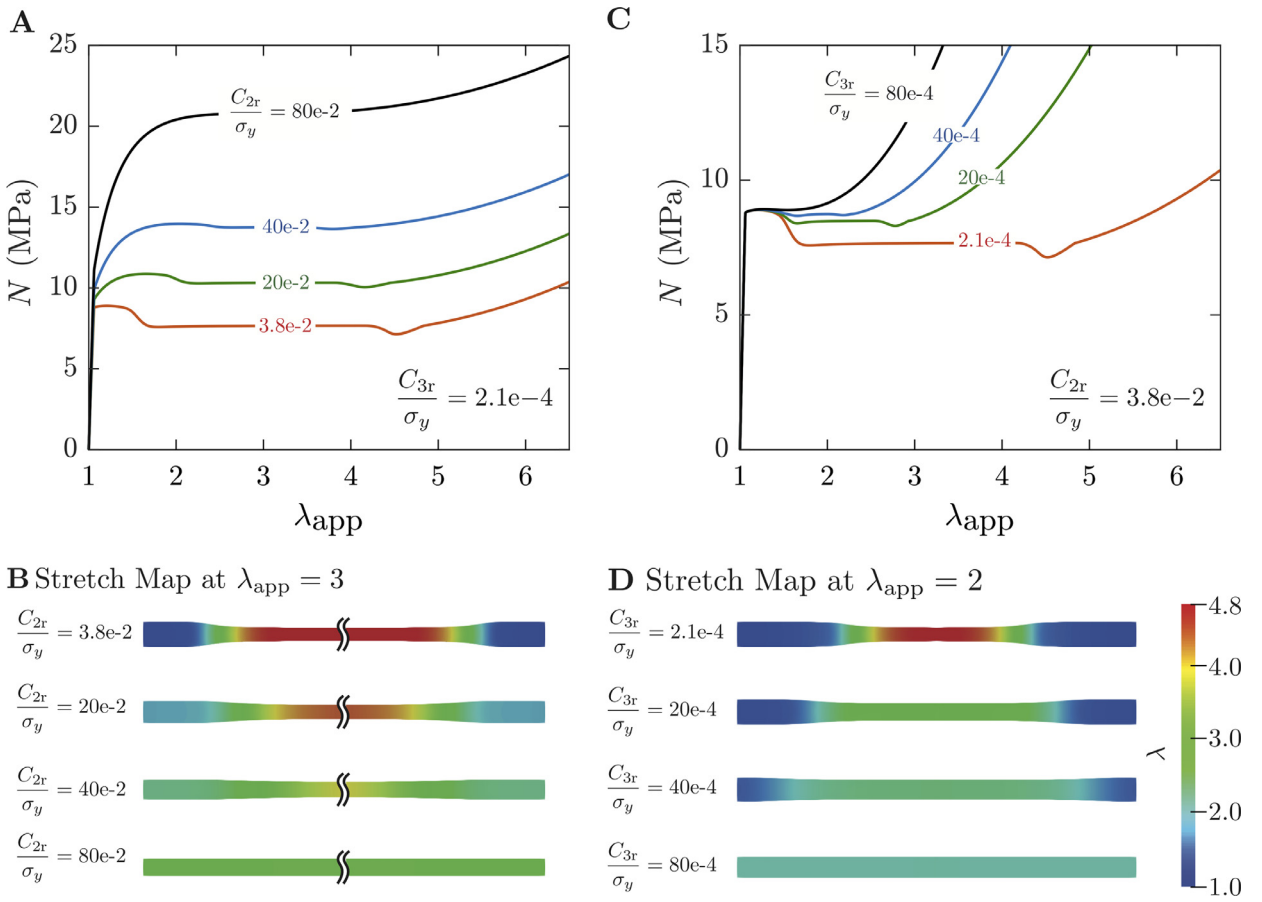

Fig. 11. (A,B): Engineering stresses and deformed shapes for laminate composites at $\lambda_{app} = 3$ with $\omega = 1$ as the C_{2r} value is changed keeping $C_{3r} = 0.004\ MPa = 0.00021\ \times \sigma_y$. (C&D): C_{3r} value is changed while keeping $C_{2r} = 0.7\ MPa = 0.038\ \times \sigma_y$. The deformed configuration is shown at a $\lambda_{app} = 2$. The orange solid curves are identical to the orange curve in Fig. 5.

rubber thickness (Fig. 5): increasing these parameters reduces the non-homogeneity of deformation (necking appears at a higher applied stretch; λ_{neck} decreases; λ_{unneck} increases) and the nominal draw stress increases. At sufficiently high values of C_{2r} and C_{3r}, necking is eliminated altogether.

There are however quantitative differences between the effects of these two parameters, which can be seen by plotting the four key metrics, λ_{peak}, λ_{neck}, λ_{unneck} and N_{draw}, against C_{2r} and C_{3r} (Fig. 12). It is clear that the stretch at which the neck appears, λ_{unneck} and N_{draw} all increase significantly as C_{2r} increases, whereas these same quantities are fairly insensitive to C_{3r}. In contrast, the stretch of the necked region, λ_{neck}, is strongly sensitive to C_{3r}. The reasons for these trends are evident from Eq. (1), the constitutive behavior for the rubber in uniaxial tension. With a series expansion at small strains, it can be shown that

$$\sigma_r = (6C_{2r} - 48C_{3r})(\lambda - 1) + \mathcal{O}\left((\lambda - 1)^2\right) \tag{12}$$

i.e. the tensile modulus is $(6C_{2r} - 48C_{3r})$. Since the C_{2r} values in Fig. 12 are typically two orders of magnitude higher than C_{3r} values, the tensile modulus, and hence the small-strain behavior, is almost entirely dominated by C_{2r}. Since the neck usually initiates at small stretch values, and λ_{unneck} is also usually small, both these are fairly insensitive to C_{3r}. On the other hand, at large stretch, the terms containing $1/\lambda$ in Eq. (1) become less important and hence the large strain behavior is dominated by C_{3r}. More specifically, as increasing C_{3r} makes the rubber more strain hardening, it strongly resists large deformation, and hence the λ_{neck} value reduces sharply.

Finally, we also calculated these four quantities using the models of Section 4.1 and 4.2 and those predictions are shown as solid lines in Fig. 12. Broadly, the conclusions remain the same as in the previous two sections: Eq. (7) along with the Maxwell construction method gives excellent predictions for λ_{peak}, λ_{neck}, and N_{draw}. However, λ_{unneck} is significantly underpredicted by the Maxwell construction and slightly underpredicted by the correction for irreversible deformation illustrated in Fig. 10.

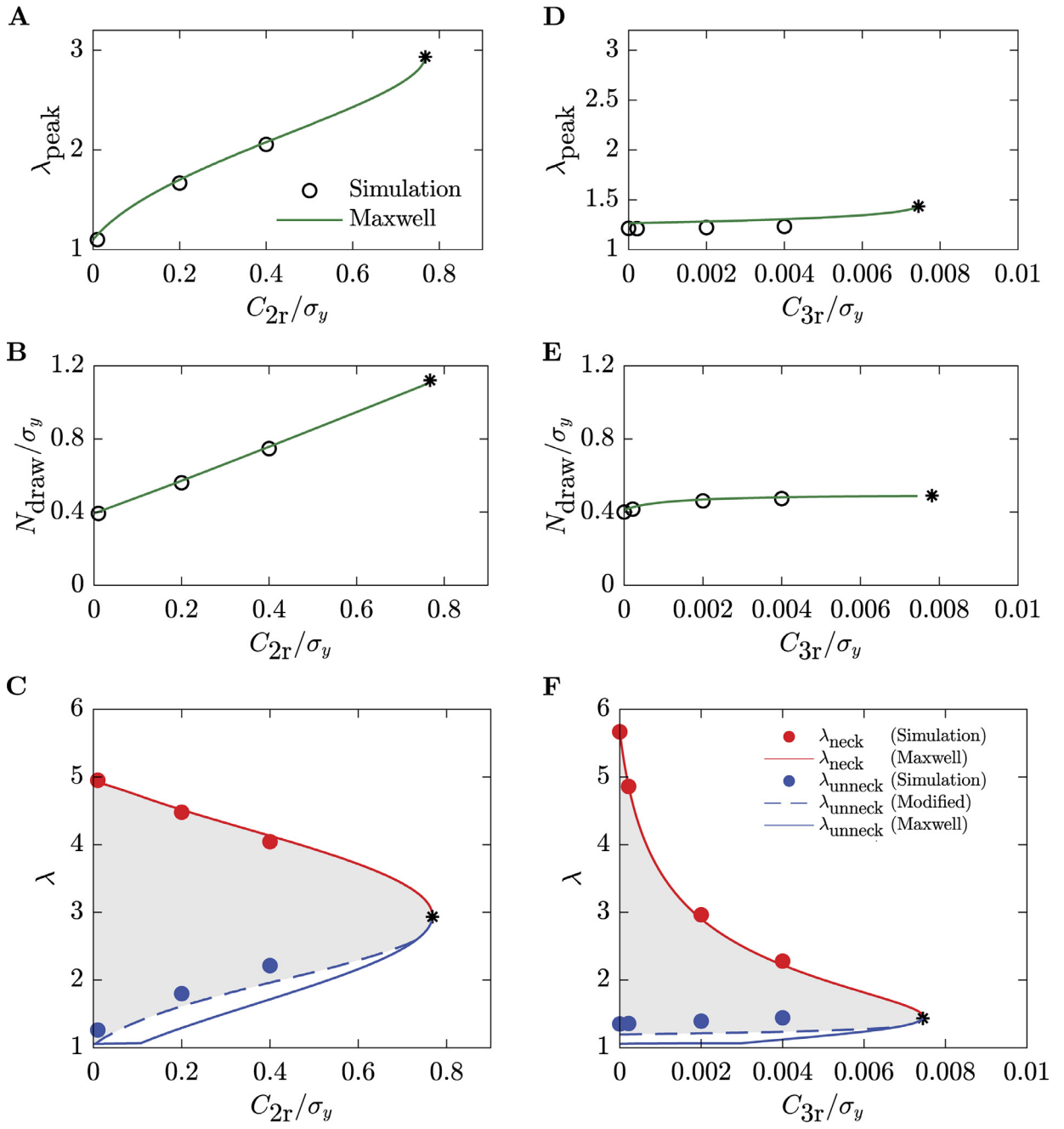

Fig. 12. Parameters extracted from the simulations of the previous Fig. 11. Solid lines in A and D are the location of the maximum PK1 stress in Eq. (7). Solid lines in B, C, E, F are predictions of Maxwell construction as applied to Eq. (7). The dashed line in C and F are the modification described in Section 4.2.

4.4. Practical relevance

The first practical message from the previous sections is that a rubber layer can altogether eliminate the necking of the plastic. The analytical model offers a simple way to estimate the thickness of rubber needed (i.e. the ω value needed) to enforce homogeneous deformation: ω_c is the minimum rubber-plastic thickness ratio (ω) required to make the nominal stress response monotonic. Appendix (Eqs. (A2)–(12)) proves that for a given plastic, the quantities $\omega_c C_{2r}$ and λ_c do not depend on C_{2r} and C_{3r} separately, but on the ratio C_{3r}/C_{2r}. Thus master curves of $\omega_c C_{2r}/\sigma_y$ and λ_c vs C_{3r}/C_{2r} can be constructed readily (Fig. 13), and ω_c needed for from any choice of rubber can be identified. For example, at fixed C_{2r}, Fig. 13A shows that ω_c reduces strongly with increasing C_{3r}/C_{2r} at small values of C_{3r}/C_{2r}. Recognizing that the modulus is almost entirely

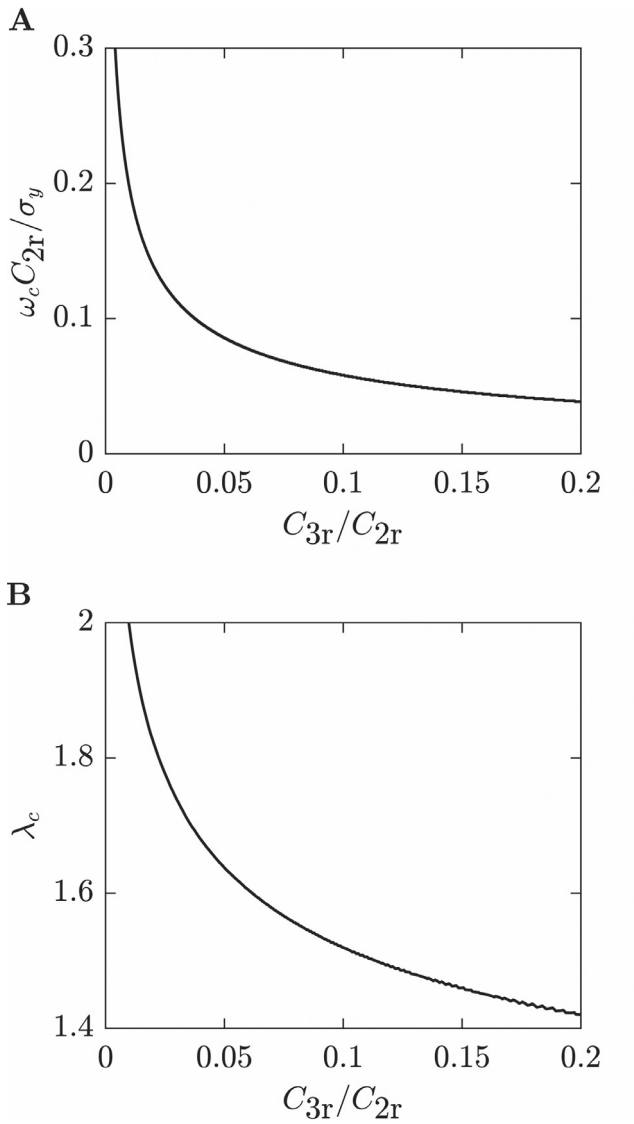

Fig. 13. (A) The minimum rubber/plastic ratio to avoid necking (ω_c) in scaled form (see text) and (B) the corresponding critical stretch λ_c, both plotted against the ratio of two rubber material parameters C_{3r}/C_{2r}.

determined by C_{2r} (Eq. (12)), this means that at fixed modulus, if the rubber is even slightly strain hardening, a small rubber thickness is sufficient to eliminate necking.

In fact, bonding a rubber layer may be useful for improving the failure resistance of the plastic layer even if necking is not completely eliminated. To illustrate this, Fig. 14A redraws the state diagram of Fig. 7C but superposes the Von Mises effective stress in the plastic layer as a color map. Here the effective stress is calculated as:

$$\sigma_{e,p}(\lambda_{app}) = \begin{cases} \sigma_p(\lambda_{app}), & if\ \lambda_{app} < \lambda_{peak}\ i.e.\ homogenous\ deformation \\ \sigma_p(\lambda_{neck}), & if\ \lambda_{peak} \le \lambda_{app} \le \lambda_{neck}\ i.e.\ necked\ state \\ \sigma_p(\lambda_{app}), & if\ \lambda_{app} > \lambda_{peak}\ i.e.\ homogenous\ deformation \end{cases} \tag{13}$$

Outside of the stable drawing envelope, deformation is homogeneous and hence the constant-stress contours are horizontal because stress only depends on the applied stretch. In contrast, inside the envelope where the material bifurcates into two coexisting phases, the constant-stress contours are vertical since they do not depend on the applied stretch, but only on the material and geometric properties.

Consider now a plastic with a failure stress of $\sigma_{e,p} = 60$ MPa, a value that exceeds the stress in the necked region of a free-standing plastic layer. Accordingly, a free-standing plastic layer fails as soon as the neck initiates, i.e. at only a few percent strain. Bonding a rubber layer reduces the stress in the plastic, and Fig. 14A shows that at $\omega = 1.1$, the stress in the

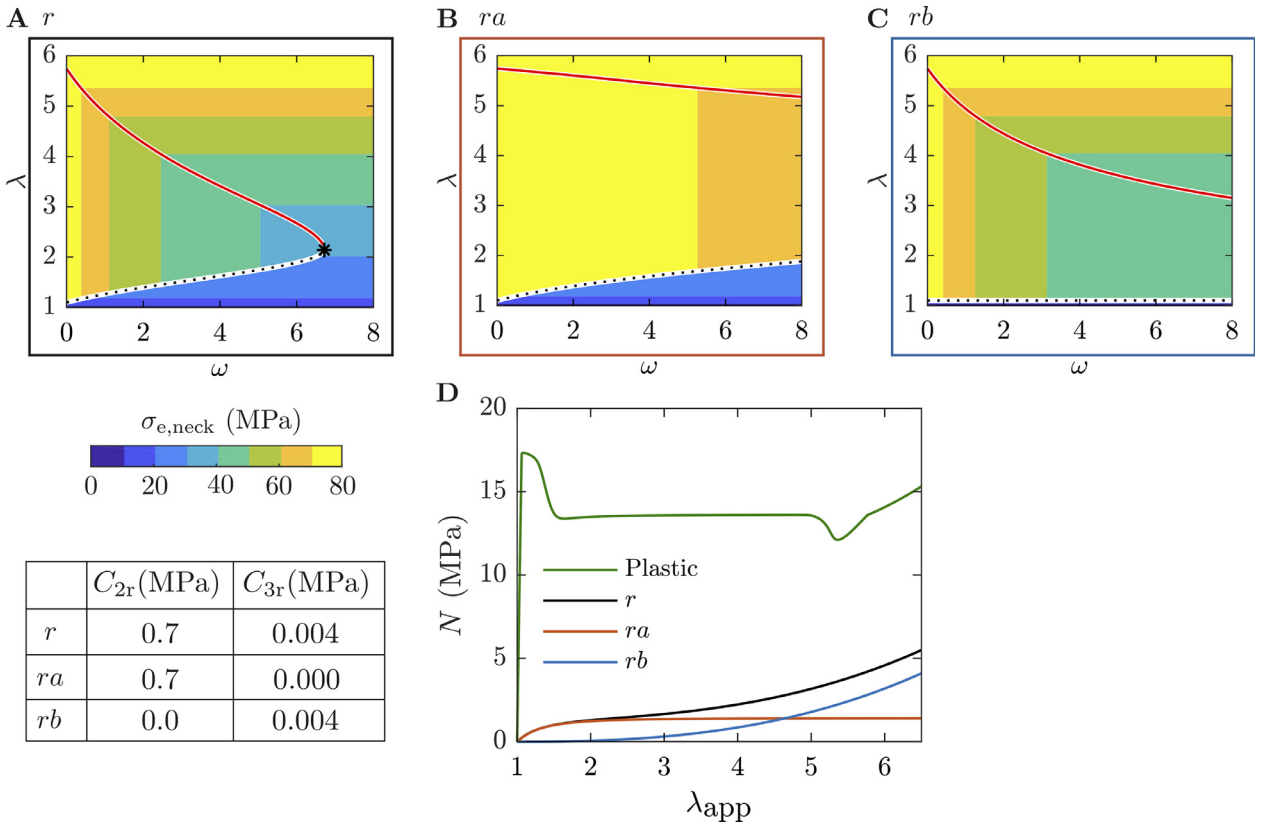

	C_{2r}(MPa)	C_{3r}(MPa)
r	0.7	0.004
ra	0.7	0.000
rb	0.0	0.004

Fig. 14. (A, B, C) Envelope of stable drawing for rubber/plastic composites with three different rubbers of properties in the table. (D) Engineering stress–strain behavior of the three rubbers.

plastic layer during stable drawing is below the adopted failure value. Thus, rubber bonding may be an effective toughening mechanism, i.e. may force ductile deformation in a plastic that is relatively brittle.

Finally, the ability of the rubber layer to reduce stress in the plastic depends almost entirely on the strain hardening characteristics of the rubber at large strain, not on its small strain behavior. This is illustrated in Fig. 14B–D. Fig. 14D shows the nominal stress–strain behaviors of three different rubbers dubbed *r, ra*, and *rb*. The rubber material properties C_{2r} and C_{3r} are listed in Fig. 14. The rubber *r* corresponds to the same properties as used in most of this paper. The rubber *ra* has nearly the same modulus as *r* but no strain hardening, whereas *rb* has the same strain hardening behavior as *r*, but zero C_{2r}.

Fig. 14B and C shows the boundaries of the coexistence regions for *ra* and *rb* respectively. The minimum rubber thickness value needed to avoid the necking of the plastic layer are seen to be $\omega = 29.9$ for *ra* and $\omega = 98.4$ for *rb*. i.e. both these rubbers require a large thickness to eliminate necking. However, to avoid failure (i.e. keep $\sigma_{p,eff} = 60$ *MPa*), the ω values needed are 39.3 for *ra* and 1.4 for *rb*; the latter value is not much larger than for the rubber *r*, which was 1.1. Clearly, reducing the degree of strain hardening of the rubber greatly increases the rubber thickness needed to avoid failure, whereas reducing the rubber modulus has little effect. This is not surprising: since λ_{neck} values for the plastic are quite high, the low-strain behavior of the rubber does not play a significant role. Indeed, some polymeric plastics can have λ_{neck} values exceeding 10 (Andrews and Ward, 1970; Seguela, 2007), especially at elevated temperatures. In such situations, the rubber would be forced into an extremely high-strain state, and even very thin rubber layers may significantly reduce the stress in the plastic. In summary, for improving failure resistance during drawing, one needs to add a layer with high large strain-strain hardening, whereas its small strain behavior is nearly irrelevant.

5. Summary and conclusions

We adapted an energy-based model, originally developed to capture the behavior of unsupported plastics, to rubber-plastic laminate composites. This model quantitatively captured some of the key parameters predicted by the simulations, including the engineering stress (or force) needed for drawing, the stretch at which the neck first appeared, and the stretch of the necked region during stable propagation. However, because the model ignores inelastic deformation (i.e. plasticity), it underpredicts the stretch of the unnecked region. An improved prediction was obtained by including the ef-

fects of irreversible deformation explicitly in the energy model. The results from finite element simulations validate the model.

The two most interesting insights from this article are

(1) The stable drawing behavior of the laminate composites can be regarded as the coexistence of two states, analogous to the thermodynamic phase transition that ends in a critical point. The envelope of this two-state region as layer thickness is varied strongly resembles a typical two-phase region, e.g. of a gas-liquid transition.
(2) Strain hardening rubber layer can reduce the stress in the plastic layer, even when the rubber is too thin to eliminate necking. Therefore, even a modest amount of elastomer may inhibit failure of the plastic layer during drawing.

Author statement

Rahul G. Ramachandran: Methodology, Computation, Writing. Spandan Maiti: Finite Element Expertise and Software, Validation. Sachin Velankar: Conceptualization, Supervision, Writing

Declaration of Competing Interest

The authors declare that they have no known competing financial interests or personal relationships that could have appeared to influence the work reported in this paper.

Acknowledgments

This research was supported by the grant NSF-CMMI-1636064 and NSF-CMMI-1561789. We are grateful to Dr. J. Carr and Dr. R. Krishnaswamy from Braskem Pittsburgh for discussions.

Appendix

Rule of mixtures using force in free-standing layers

Thickness-weighted sum of the force in each free-standing layer gives:

$$F = wh_{\mathrm{p}}F_{\mathrm{p}} + wh_{\mathrm{r}}F_{\mathrm{r}}$$

which can be re-written as

$$N = N_{\mathrm{p}}\left(\frac{1}{\omega+1}\right) + N_{\mathrm{r}}\left(\frac{\omega}{\omega+1}\right). \tag{A1}$$

In this equation, $N = \frac{F}{w(h_{\mathrm{p}}+h_{\mathrm{r}})}$ is the nominal stress in the laminate composite, whereas $N_{\mathrm{p}} = \frac{F_{\mathrm{p}}}{wh_{\mathrm{p}}}$ and $N_{\mathrm{r}} = \frac{F_{\mathrm{r}}}{wh_{\mathrm{r}}}$ are the nominal stresses in the free-standing plastic and rubber respectively. Such a force-additivity rule of mixtures is convenient experimentally since it can be constructed from measured forces without needing to assume any specific constitutive behavior for each material. In contrast, Eq. (7) in the main text requires knowledge of the constitutive behavior since it is the PK1 stresses that are added.

Appendix Fig. A1 shows that Eq. (A1) tracks the nominal stress curves approximately, but with significant and systematic deviations over much of the stretch range. Most obviously the nominal stress from the simulation shows a much broader peak and a completely flat plateau, neither of which are captured correctly by Eq. (A1).

This deviation is not surprising since the assumption underlying Eq. (A1) is that the two materials are stretched in parallel with no interaction between the layers. Therefore, the plastic and rubber layers can be in different stretch states, and in particular, Eq. (A1) adds together the forces from a free-standing plastic layer that deforms non-homogeneously and a free-standing rubber layer that stretches homogeneously. In contrast, the simulation imposes perfect bonding between the layers and hence equal stretch in both layers. Accordingly, over a wide range of stretch values, the free-standing plastic, the free-standing rubber, and the composite are all in different stretch states, thus a simple addition of forces does not give an accurate prediction.

Scaling of the critical point with ratio of the rubber parameters

In the article, we constructed the PK1 (P) stress for the composite as a weighted average of the rubber and plastic:

$$P = \left(\frac{1}{\omega+1}\right)P_p(\lambda) + \left(\frac{\omega}{\omega+1}\right)P_r(C_{2\mathrm{r}}, C_{3\mathrm{r}}, \lambda) \tag{A2}$$

In the above, P_p is denoted as a function of λ alone to indicate that for the following analysis, the parameters of the plastic are taken as a constant. The first two derivatives are each set to zero:

$$\frac{\partial P_p(\lambda_c)}{\partial\lambda}\left(\frac{1}{\omega_c+1}\right) + \frac{\partial P_r(C_{2\mathrm{r}}, C_{3\mathrm{r}}, \lambda_c)}{\partial\lambda}\left(\frac{\omega_c}{\omega_c+1}\right) = 0 \tag{A3}$$

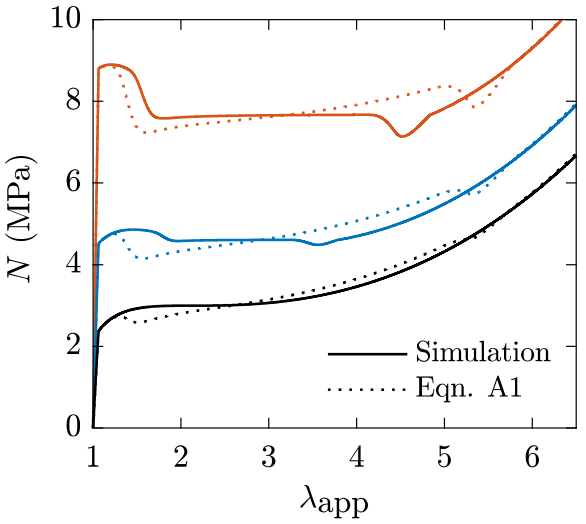

Fig. A1. Solid lines are the simulated nominal stress response for cold drawing plastic- rubber trilayer laminates of $\omega = 1, 3$ and 7 (same data as in Fig. 5A). The dotted lines are the rule of mixture prediction based on the nominal stress behavior of individual free-standing layers (Eq. (A1)).

$$\frac{\partial^2 P_p(\lambda_c)}{\partial \lambda^2}\left(\frac{1}{\omega_c+1}\right)+\frac{\partial^2 P_r(C_{2r},C_{3r},\lambda_c)}{\partial \lambda^2}\left(\frac{\omega_c}{\omega_c+1}\right)=0 \tag{A4}$$

The above two equations give two expressions for ω_c,

$$\omega_c=-\frac{\frac{\partial P_p(\lambda_c)}{\partial \lambda}}{\frac{\partial P_r(C_{2r},C_{3r},\lambda_c)}{\partial \lambda}} \text{ and } \omega_c=-\frac{\frac{\partial^2 P_p(\lambda_c)}{\partial^2 \lambda}}{\frac{\partial^2 P_r(C_{2r},C_{3r},\lambda_c)}{\partial^2 \lambda}} \tag{A5}$$

These two equations can be equated to eliminate ω_c and rearranging,

$$\frac{\frac{\partial P_r(C_{2r},C_{3r},\lambda_c)}{\partial \lambda}}{\frac{\partial^2 P_r(C_{2r},C_{3r},\lambda_c)}{\partial \lambda^2}}=\frac{\frac{\partial P_p(\lambda_c)}{\partial \lambda}}{\frac{\partial^2 P_p(\lambda_c)}{\partial \lambda^2}}=f_1(\lambda_c) \tag{A6}$$

where $f_1(\lambda_c)$ is a function of λ_c alone. While $f_1(\lambda_c)$ can be evaluated from the expression P_p given in the text, for the present purposes, it is not necessary to evaluate it explicitly. We can relate, C_{2r}, C_{3r} and λ through the constitutive relation as follows:

$$P_r(C_{2r},C_{3r},\lambda)=\left[2C_{2r}\lambda^{-1}+4C_{3r}\left(\lambda^2-2\lambda^{-1}-3\right)\right]\left(\lambda-\lambda^{-2}\right) \tag{A7}$$

Taking the first and second order partial derivative of P_r with λ and substituting in Eq. (A6),

$$\frac{\frac{\partial P_r(C_{2r},C_{3r},\lambda_c)}{\partial \lambda}}{\frac{\partial^2 P_r(C_{2r},C_{3r},\lambda_c)}{\partial \lambda^2}}=\frac{-C_{2r}\lambda_c^{-4}+2C_{3r}\left(\lambda_c^2-2\lambda_c^{-4}-2\lambda_c^{-3}-1\right)}{4C_{2r}\lambda_c^{-5}+4C_{3r}\left(\lambda_c+4\lambda_c^{-5}+3\lambda_c^{-4}\right)}=f_1(\lambda_c)$$

$$\text{which gives, } \frac{-\lambda_c+\frac{2C_{3r}}{C_{2r}}\left(\lambda_c^7-2\lambda_c-2\lambda_c^2-\lambda_c^5\right)}{4+\frac{4C_{3r}}{C_{2r}}\left(\lambda_c^6+4+3\lambda_c\right)}=f_1(\lambda_c) \tag{A8}$$

Rearranging,

$$\frac{C_{3r}}{C_{2r}}=\frac{4f_1(\lambda_c)+\lambda_c}{2\left[\lambda_c^7-2\lambda_c-2\lambda_c^2-\lambda_c^5-2\left(\lambda_c^6+4+3\lambda_c\right)f_1(\lambda_c)\right]}=f_2(\lambda_c) \tag{A9}$$

where $f_2(\lambda_c)$ is a function in λ_c alone. This shows that λ_c depends on the ratio $\frac{C_{3r}}{C_{2r}}$, and not on C_{2r} and C_{3r} separately, justifying the plot of Fig. 2B in the main text.

Returning to the equation for ω_c

$$\omega_c=-\frac{\frac{\partial P_p(\lambda_c)}{\partial \lambda}}{\frac{\partial P_r(C_{2r},C_{3r},\lambda_c)}{\partial \lambda}}=-\frac{\frac{\partial P_p(\lambda_c)}{\partial \lambda}}{-C_{2r}\lambda_c^{-4}+2C_{3r}\left(\lambda_c^2-2\lambda_c^{-4}-2\lambda_c^{-3}-1\right)} \tag{A10}$$

Therefore,

$$\omega_c C_{2r} = -\frac{\frac{\partial P_p(\lambda_c)}{\partial \lambda}}{-\lambda_c^{-4} + \frac{2C_{3r}}{C_{2r}}\left(\lambda_c^2 - 2\lambda_c^{-4} - 2\lambda_c^{-3} - 1\right)} \tag{A11}$$

Since λ_c has one-to-one relation with $\frac{C_{3r}}{C_{2r}}$, the form of the above equation is

$$\omega_c C_{2r} = f_3(\lambda) = f_4\left(\frac{C_{3r}}{C_{2r}}\right) \tag{A12}$$

This shows that $\omega_c C_{2r}$ depends on the ratio C_{2r}/C_{3r} and not on C_{3r} and C_{2r} separately, justifying Fig. 13A in the main text.

Experimental and simulated engineering stress – applied stretch curves

Determination of stretch in the necked and unnecked regions

Critical exponent

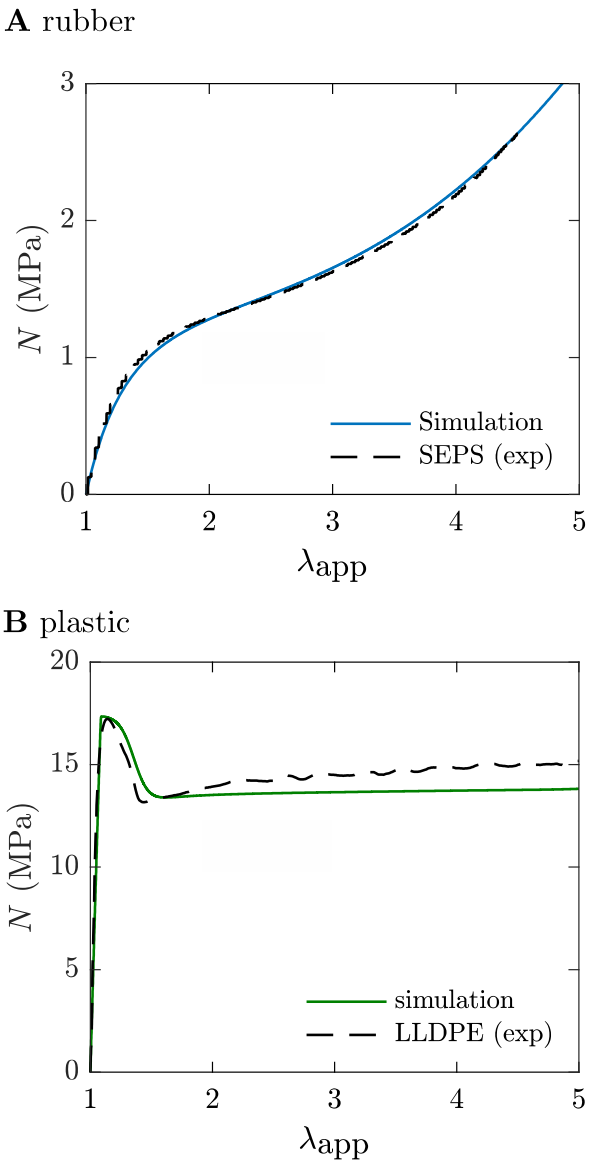

Fig. A2. Simulated (sold curves) and experimentally obtained (dashed curves) engineering stress-applied stretch curve for (a) SEPS rubber and (b) LLDPE.

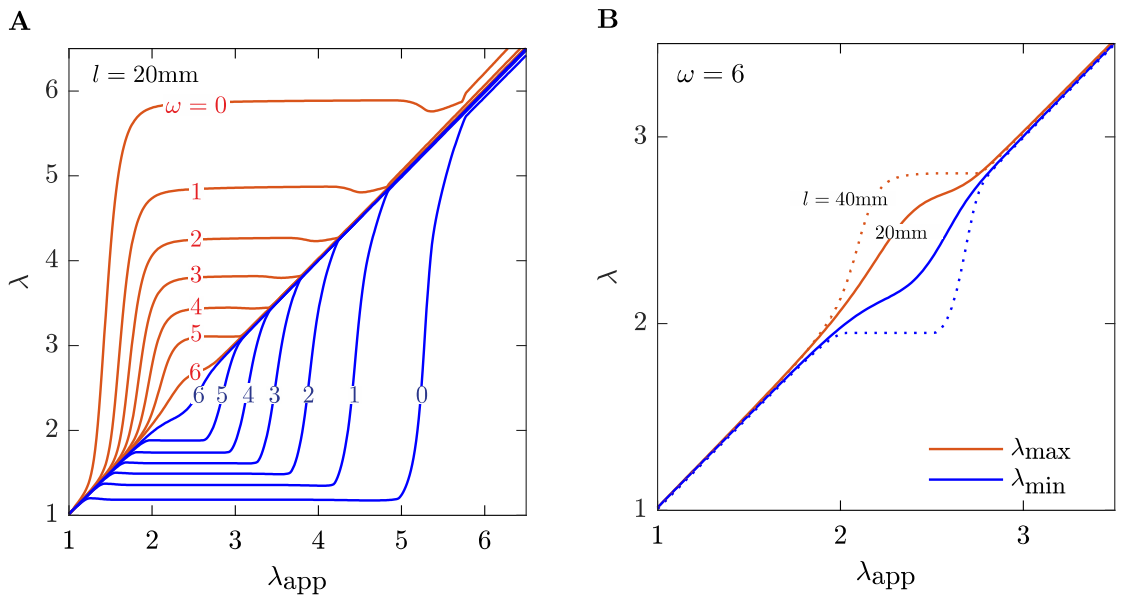

Fig. A3. (A) Maximum and minimum values of stretch within each specimen during the stretching process. The specimen length is 20 mm. The diagonal $\lambda = \lambda_{app}$ line represents homogeneous deformation. Simulations with $\omega \leq 5$ show clear plateaus in λ_{max} and λ_{min}, which are respectively taken as λ_{neck} and λ_{unneck} respectively. Simulations with $\omega > 6.7$ show no deviation from the diagonal, i.e. homogeneous deformation. The simulation with $\omega = 6$ does not show clear plateaus in λ_{max} and λ_{min} because the deformation is nearly homogeneous. Specifically, the neck evolves very gradually, and hence the entire sample reverts to homogeneity before stable drawing can be established. This is a finite-length effect, as illustrated in B. (B) Simulation with $\omega = 6$ conducted with two different simulation lengths keeping the width and thickness fixed. The longer geometry gives clear plateaus in λ_{max} and λ_{min}. For this ω value, the longer simulation geometry was used to obtain λ_{neck} and λ_{unneck}.

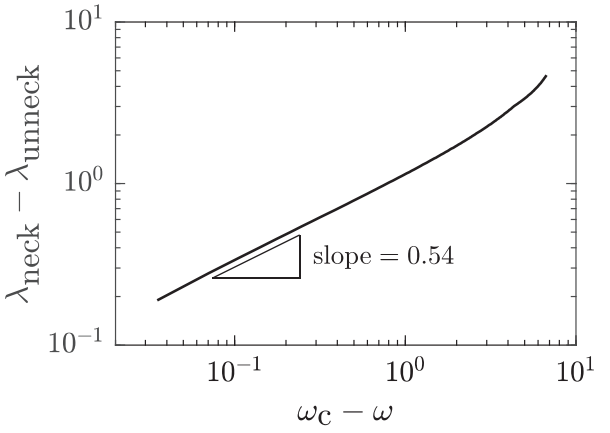

Fig. A4. The predictions of the Maxwell construction (same as λ_{neck} and λ_{unneck} values as from Fig. 7C) redrawn in the form suitable for second-order phase transitions.

References

Andrews, J.M., Ward, I.M., 1970. Cold-drawing of high density polyethylene. J. Mater. Sci. 5, 411–417.
Argon, A.S., 2013a. The physics of deformation and fracture of polymers- instabilities in extensional plastic flow. The Physics of Deformation and Fracture of Polymers. Cambridge University Press.
Argon, A.S., 2013b. The physics of deformation and fracture of polymers- plasticity og glassy polymers and plasticity of semi crystalline polymers. The Physics of Deformation and Fracture of Polymers. Cambridge University Press.
Barenblatt, G.I., 1974. Neck propagation in polymers. Rheol. Acta 13, 924–933.
Bigg, D.M., 1976. A review of techniques for processing ultra high modulus polymers. Plolym. Eng. Sci. 16, 725–734.
Carothers, W.H., Hills, J.W., 1932. Studies of Polymerization and ring formation. XV. Artificial fibres from synthetic linear condensation superpolymers. J. Am. Chem. Soc. 54, 1579.
Coates, P.D., Ward, I.M., 1978. The plastic deformation behaviour of linear polyethylene and polyoxymethylene. J. Mater. Sci. 13, 1957–1970.
Coates, P.D., Ward, I.M., 1980. Neck profiles in drawn linear polyethylene. J. Mater. Sci. 15, 2897–2914.
Coleman, B.D., 1983. Necking and drawing in polymeric fibers under tension. Arch. Ration. Mech. Anal. 83, 115–137.
Considère, A.G., 1885. Annales P. 9, 574–775.
Courtney, T.H., 1990. Mechanical Behavior of Materials, Mechanical Behavior of Materials. Waveland Press, Illinois, pp. 20–30.

Crist, B., Metaxas, C., 2004. Neck propagation in polyethylene. J. Polym. Sci. Pt. B – Polym. Phys. 42, 2081–2091.
Erickson, J.L., 1975. Equilibrium of bars. J. Elast. 5, 191–201.
Fager, L.O., Bassani, J.L., 1986. Plane strain neck propagation. Int. J. Solids Struct. 22, 1243–1257.
Gsell, C., Jonas, J.J., 1979. Determination of the plastic behavior of solid polymers at constant true strain rate. J. Mater. Sci. 14, 583–591.
Hutchinson, J.W., 2014. Necking modes in multilayers and their influence on tearing toughness. Math. Mech. Solids 19, 39–55.
Hutchinson, J.W., Miles, J.P., 1974. Bifurcation analysis of onset of necking in an elastic-plastic cylinder under uniaxial tension. J. Mech. Phys. Solids 22, 61–71.
Hutchinson, J.W., Neale, K.W., 1977. Influence of strain-rate sensititvity on necking under uniaxial tension. Acta Metall. 25, 839–846.
Hutchinson, J.W., Neale, K.W., 1983. Neck propagation. J. Mech. Phys. Solids 31, 405–426.
Lambricht, N., Pardoen, T., Yunus, S., 2013. Giant stretchability of thin gold films on rough elastomeric substrates. Acta Mater. 61, 540–547.
Li, T., Huang, Z.Y., Suo, Z., Lacour, S.P., Wagner, S., 2004. Stretchability of thin metal films on elastomer substrates. Appl. Phys. Lett. 85, 3435–3437.
Li, T., Huang, Z.Y., Xi, Z.C., Lacour, S.P., Wagner, S., Suo, Z., 2005. Delocalizing strain in a thin metal film on a polymer substrate. Mech. Mater. 37, 261–273.
Lu, N.S., Wang, X., Suo, Z.G., Vlassak, J., 2007. Metal films on polymer substrates stretched beyond 50%. Appl. Phys. Lett. 91 221909.
Neale, K.W., Tugcu, P., 1985. Analysis of necking and neck propagation in polymeric materials. J. Mech. Phys. Solids 33, 323–337.
Ramachandran, R.G., Hariharakrishnan, S., Fortunato, R., Abramowitch, S.D., Maiti, S., Velankar, S.S., 2018. Necking and drawing of rubber-plastic bilayer laminates. Soft Matter 14, 4977–4986.
Seguela, R., 2007. On the natural draw ratio of semi-crystalline polymers: review of the mechanical, physical and molecular aspects. Macromol. Mater. Eng. 292, 235–244.
Vincent, P.I., 1960. The necking and cold-drawing of rigid plastics. Polymer 1, 7–19.
Yang, J., Damle, S., Maiti, S., Velankar, S.S., 2017. Stretching-induced wrinkling in plastic-rubber composites. Soft Matter 13, 776–787.